The Effects of Mesoscale Ocean–Atmosphere Coupling on the Large-Scale Ocean Circulation

ANDREW MCC. HOGG

Australian National University, Canberra, Australian Capital Territory, Australia

WILLIAM K. DEWAR

The Florida State University, Tallahassee, Florida

PAVEL BERLOFF

Woods Hole Oceanographic Institution, Woods Hole, Massachusetts, and Cambridge University, Cambridge, United Kingdom

SERGEY KRAVTSOV

University of Wisconsin—Milwaukee, Milwaukee, Wisconsin

DAVID K. HUTCHINSON

Australian National University, Canberra, Australian Capital Territory, Australia

(Manuscript received 13 May 2008, in final form 24 February 2009)

ABSTRACT

Small-scale variation in wind stress due to ocean–atmosphere interaction within the atmospheric boundary layer alters the temporal and spatial scale of Ekman pumping driving the double-gyre circulation of the ocean. A high-resolution quasigeostrophic (QG) ocean model, coupled to a dynamic atmospheric mixed layer, is used to demonstrate that, despite the small spatial scale of the Ekman-pumping anomalies, this phenomenon significantly modifies the large-scale ocean circulation. The primary effect is to decrease the strength of the nonlinear component of the gyre circulation by approximately 30%–40%. This result is due to the highest transient Ekman-pumping anomalies destabilizing the flow in a dynamically sensitive region close to the western boundary current separation. The instability of the jet produces a flux of potential vorticity between the two gyres that acts to weaken both gyres.

1. Introduction

Recent satellite observations have shown that the stress on the surface of the ocean varies on the relatively fine spatial scales governed by oceanic mesoscale dynamics. This spatial variability can be attributed primarily to a combination of the dependence of stress upon ocean velocity (Chelton et al. 2004; Park et al. 2006; Liu et al. 2007) and patterns of sea surface temperature (SST) variations (Nonaka and Xie 2003; Chelton et al. 2004; Xie 2004). In this paper we focus upon the latter of these two effects and, in particular, whether mesoscale coupling of SST and wind stress can alter the large-scale (i.e., basin scale) ocean circulation.

SST variations are greatest in regions of strong fronts or where eddies cause rapid changes in SST in the along wind direction (Spall 2007b). Prime candidate areas for strong mesoscale coupling include the tropical Pacific and Atlantic Oceans where tropical instability waves occur and near western boundary-current (WBC) separation regions where eddies and fronts are most active. These regions are analyzed in a recent review article (Small et al. 2008) that summarizes the known processes contributing to mesoscale wind stress variability. The dynamics leading to correlations between the spatial

Corresponding author address: Andrew McC. Hogg, Research School of Earth Sciences, Australian National University, Canberra, ACT 0200, Australia.
E-mail: andy.hogg@anu.edu.au

DOI: 10.1175/2009JCLI2629.1

variability of wind stress and SST is subtle, and there are a number of possible contributing factors including vertical mixing of momentum, changes in the planetary boundary layer depth, a secondary atmospheric response due to pressure gradients within the boundary layer, and changes in cloud cover across the fronts.

When the sea surface is warmer than the atmospheric boundary layer, excessive convective mixing will magnify vertical eddy momentum flux and hence enhance stress close to the sea surface (Sweet et al. 1981). Samelson et al. (2006) argue, with support from analytical models, that the convective mixing mechanism will result in enhanced wind stress over warmer water, but that the reverse situation requires an aphysical ''upward unmixing.'' They imply that the primary effect on stress is therefore due to the effect of convective mixing upon the depth of the atmospheric boundary layer. Spall (2007b) uses an idealized model to confirm the role of the boundary layer thickness in governing stress for the case of equilibrium winds (i.e., far from fronts where gradients of SST are large) but points out that the linear relationship between the boundary layer thickness and stress breaks down in the immediate vicinity of the front. The horizontal momentum balance in these model simulations emphasizes the role of turbulent vertical mixing as the rapid response mechanism to SST gradients.

An alternative hypothesis to explain mesoscale variations in wind stress is that of pressure gradients induced by the SST patterns (Lindzen and Nigam 1987). This hypothesis has been confirmed using recent observations (Cronin et al. 2003) and numerical simulations (Small et al. 2003, 2005) in the tropical Pacific, although the possibility of vertical mixing contributing to the momentum balance in those cases has not been ruled out. In addition, the drag coefficient itself can vary with temperature, although this effect is expected to be second order (O'Neill et al. 2005; Spall 2007b).

In their review article, Small et al. (2008) point out that a single, universally acknowledged mechanism for small-scale wind stress variations does not exist. Instead, it appears that a combination of different processes contributes. For example, if strong winds cross a sharp front, the air temperature does not have time to respond to SST and thus vertical mixing of momentum dominates over pressure gradients (Spall 2007b). Conversely, if winds are weak, then the air temperature has time to equilibrate to SST, and the air pressure response may dominate. Furthermore, the role of vertical turbulent mixing is different for the case of a warm-to-cold front, implying that either the Coriolis effect (Spall 2007b) or the boundary layer height reduction (Samelson et al. 2006) is responsible for the reduction in stress near the front.

Thus, it appears likely that different mechanisms operate in different regions, depending upon the strength of the front and the strength and direction of the large-scale winds. It is therefore surprising that satellite observations yield a simple statistical relationship between wind stress and SST: namely, that wind stress divergence is linearly proportional to the downwind SST gradient, while wind stress curl is proportional to the crosswind SST gradient (Chelton et al. 2004). This relationship was initially observed in the eastern tropical Pacific (Chelton et al. 2001), but also applies in the Southern Ocean (O'Neill et al. 2003, 2005) as well as the Kuroshio and Gulf Stream (Chelton et al. 2004). While the constant of proportionality varies in each case (presumably owing to variations in the operating mechanisms), a universal pattern is that the constant is approximately twice as large for the divergence as for the curl. This covariation suggests that a relatively simple parameterization may be able to capture the essential dynamics of this process.

The dependence of wind stress curl upon crosswind temperature gradients means that large values of transient, small-scale Ekman pumping are expected. Ekman pumping plays a first-order role in driving ocean currents, and mesoscale coupling is therefore likely to have an effect on local flow, raising the prospect of further feedback onto ocean circulation. For example, it was established by Dewar and Flierl (1987) that variations in Ekman pumping may have small-scale local effects on steering and dissipating Gulf Stream rings. Modeling of the North Atlantic gyre system showed that high frequency perturbations to the wind stress curl enhanced both the mean and eddy kinetic energy in the eastern part of the gyre (Milliff et al. 1996). Spall (2007a) proposes that feedback between fronts and the atmospheric boundary layer will enhance the growth rates of baroclinic instability on those fronts, thereby affecting the ocean circulation. The possibility for dynamic feedback with the ocean was demonstrated using a high-resolution regional coupled model of the tropical Pacific (Seo et al. 2007). Here, the growth rate of tropical instability waves was damped by this feedback process.

The results of Milliff et al. (1996) and Seo et al. (2007) indicate that mesoscale coupling may feed back on the ocean circulation to produce effects that are not merely local. However, Milliff et al. (1996) used a forcing that represented the wind stress variations statistically, rather than dynamically, while Seo et al. (2007) concentrated on the tropical ocean dynamics. In this paper we ask the question: can mesoscale coupled feedback act to modify the large-scale midlatitude ocean gyre circulation? To answer this question we use an idealized coupled ocean–atmosphere model that resolves ocean

eddies. The model (described in section 2) includes a simple, first-order parameterization for mesoscale coupling. We first test this parameterization to determine whether it produces correlations between mesoscale wind stress patterns and SST that are consistent with satellite observations. Then we conduct numerical experiments to determine the nature and cause of the large-scale oceanic response to mesoscale coupling and demonstrate the operating dynamics with a conceptual low-order model for interaction.

2. Model

We use a quasigeostrophic coupled model (Q-GCM) (Hogg et al. 2003b) that is designed to model the ocean at eddy-resolving scales in a coupled setting. Q-GCM is an idealized model with three quasigeostrophic ocean layers—the reduced layer representation allows the model to be run efficiently at very high resolution, thereby permitting a number of experiments over a wide range of governing parameters. Version 1.4β of the model is used with some key modifications. In this model version, instead of the full coupling, we prescribe the geostrophic wind field to be purely zonal. The model has a dynamic atmospheric mixed layer, which enables us to calculate the evolution of the atmospheric mixed-layer temperature (AMLT) and wind stress, as well as a dynamic ocean mixed layer embedded within the first quasigeostrophic (QG) ocean layer where sea surface temperature evolution is calculated. In this version of the model we use 10-km resolution in both ocean and atmosphere to capture the dynamic effect of mesoscale eddies and the role of coupling on this scale. The model equations are summarized below; for a full description of the model see Hogg et al. (2003a).

a. Ocean dynamical core

The QG equations describing the dynamics in all parts of the three-layer ocean domain (except for the boundaries) are

$$q_{1t} = \frac{1}{f_0} J(q_1, p_1) - \frac{A_4}{f_0}\nabla_H^6 p_1 + \frac{f_0 w_{\mathrm{Ek}}}{H_1}, \tag{1}$$

$$q_{2t} = \frac{1}{f_0} J(q_2, p_2) - \frac{A_4}{f_0}\nabla_H^6 p_2, \tag{2}$$

and

$$q_{3t} = \frac{1}{f_0} J(q_3, p_3) - \frac{A_4}{f_0}\nabla_H^6 p_3 - \frac{\delta_{\mathrm{Ek}}}{2H_3}\nabla_H^2 p_3, \tag{3}$$

where p_k is the layer pressure and q_k the layer potential vorticity. Mean layer thickness is denoted H_k, while A_4 is a coefficient for biharmonic viscosity, f_0 the mean Coriolis parameter, w_{Ek} the Ekman-pumping velocity imposed by the wind stress forcing, and δ_{Ek} the Ekman-layer thickness at the bottom of layer 3. Pressure is determined at each time step from the potential vorticity by inverting

$$f_0 q_k = \nabla_H^2 p_k + f_0\beta(y - y_0) + \frac{f_0^2}{H_k}(\eta_k - \eta_{k-1}) \quad \text{for} \quad k = 1, 2, 3, \tag{4}$$

where β is the latitudinal gradient of the Coriolis parameter and we define interface height perturbations as

$$\eta_k = -\frac{p_k - p_{k+1}}{g_k'} \quad \text{for} \quad k = 1, 2, \qquad \eta_0 = \eta_3 = 0. \tag{5}$$

Here g_k' is the reduced gravity between layers k and $k + 1$.

Pressure on the boundaries is determined using boundary conditions

$$p_k = f_k(t), \tag{6}$$

where the function $f_k(t)$ is determined by mass conservation and is constant around the boundary. Boundary conditions are also required for the derivatives of pressure on all solid boundaries, and we use a mixed condition applied to the normal derivatives, following Haidvogel et al. (1992),

$$p_{knn} = -\frac{\alpha_{\mathrm{bc}}}{\Delta x} p_{kn} \tag{7}$$

and

$$p_{k4n} = -\frac{\alpha_{\mathrm{bc}}}{\Delta x} p_{k3n}, \tag{8}$$

where the nondimensional coefficient α_{bc} is zero for free-slip and infinite for no-slip boundary conditions (although, in practice, $\alpha_{\mathrm{bc}} > 2$ is a good approximation to no slip), Δx is the horizontal grid spacing, and subscript n denotes the outward normal derivative.

b. Mixed layer evolution

The evolution of the oceanic mixed layer temperature (relative to the mean temperature) ${}^oT_m$ is determined using

$${}^oT_{mt} = -({}^ou_m\,{}^oT_m)_x - ({}^o\upsilon_m\,{}^oT_m)_y + {}^oK_2\nabla_H^2\,{}^oT_m - {}^oK_4\nabla_H^4\,{}^oT_m - \frac{F_0 + F_S'}{{}^o\rho\,{}^oC_p\,{}^oH_m}, \tag{9}$$

where

$$({}^{o}u_m, {}^{o}v_m) = \frac{1}{f_0}(-p_{1y}, p_{1x}) + \frac{1}{f_0 {}^{o}H_m}({}^{o}\tau^y, -{}^{o}\tau^x) \quad (10)$$

is the mixed layer velocity and $({}^{o}\tau^x, {}^{o}\tau^y)$ the dynamic stress at the ocean surface. Note the use of both Laplacian and biharmonic diffusion with coefficients ${}^{\circ}K_2$ and ${}^{\circ}K_4$, respectively. Fluxes of heat at the surface include a steady insolation F_S' and a time-dependent ocean–atmosphere heat flux F_0, which is calculated using a linearized radiation and heat flux scheme. The heat fluxes are described in detail by Hogg et al. (2003a) but are based primarily on the sensible and latent heat flux $\lambda({}^{o}T_m - {}^{a}T_m)$ due to the ocean–atmosphere temperature difference. Boundary conditions are zero flux on all boundaries, except for the southern boundary where temperature is specified as a proxy for advection of warm tropical water into that region.

The temperature evolution the atmospheric mixed layer is given by

$$\begin{aligned} {}^{a}T_{mt} = & -({}^{a}u_m {}^{a}T_m)_x - ({}^{a}v_m {}^{a}T_m)_y + {}^{a}K_2 \nabla_H^2 {}^{a}T_m \\ & - {}^{a}K_4 \nabla_H^4 {}^{a}T_m + \frac{-F_m + F_0}{{}^{a}\rho {}^{a}C_p {}^{a}h_m}, \end{aligned} \quad (11)$$

where

$$({}^{a}u_m, {}^{a}v_m) = \frac{1}{f_0}(-{}^{a}p_{1y}, {}^{a}p_{1x}) + \frac{1}{f_0 {}^{a}H_m}(-{}^{a}\tau^y, {}^{a}\tau^x). \quad (12)$$

Here F_m is the outgoing radiative flux (derived in full by Hogg et al. 2003a), and other parameters are atmospheric equivalents of the parameters in (9). North and south boundary conditions on atmospheric temperature are zero flux, while east–west boundaries are periodic.

c. Wind stress

The standard bulk formulation for calculating wind stress in Q-GCM is

$$({}^{a}\tau^x, {}^{a}\tau^y) = C_D |{}^{\mathbf{a}}\mathbf{u}_{\mathbf{m}}| ({}^{a}u_m, {}^{a}v_m),$$

which represents the quadratic effect of wind speed on drag using a constant drag coefficient C_D (Pedlosky 1987). In this study we investigate the role of small-scale ocean–atmosphere coupling by allowing the wind stress to depend upon the temperature difference between ocean and atmosphere. This effect is parameterized in a crude way, by writing

$$({}^{a}\tau^x, {}^{a}\tau^y) = C_D(1 + \alpha \Delta T) |{}^{\mathbf{a}}\mathbf{u}_{\mathbf{m}}| ({}^{a}u_m, {}^{a}v_m), \quad (13)$$

where $\Delta T = {}^{o}T_m - {}^{a}T_m$ is the atmosphere–ocean temperature difference. In this manuscript we refer to this scheme as a *temperature-dependent wind stress*. We then calculate ocean stress from ${}^{o}\boldsymbol{\tau} = {}^{a}\rho {}^{a}\boldsymbol{\tau} / {}^{o}\rho$. Ocean Ekman-pumping velocity is calculated from ocean stress using

$$w_{\mathrm{Ek}} = \frac{1}{f_0}({}^{o}\tau_x^y - {}^{o}\tau_y^x), \quad (14)$$

which is the forcing term in (1).

d. Calibration and comparison with observations

The proposed parameterization for temperature-dependent wind stress, Eq. (13), is designed to emulate the role of convective instability driving the vertical mixing of momentum within the atmospheric boundary layer (Sweet et al. 1981; Spall 2007b). However, it is clear that more than one mechanism contributes to mesoscale wind stress variations (Samelson et al. 2006; Small et al. 2008): atmospheric boundary layer thickness and secondary pressure gradients may also play a major role. The present study is concerned not with the mechanism of stress variation but with the effect that it has on the ocean circulation. For this reason, we aim to confirm that the simple parameterization, Eq. (13), gives similar results to observations.

The most complete and robust observations of mesoscale wind stress variability come from satellite scatterometer measurements. A number of studies have shown a linear correlation between downwind (crosswind) SST gradients and wind stress divergence (curl) (Chelton et al. 2001; O'Neill et al. 2003; Chelton et al. 2004; O'Neill et al. 2005). These data provide a solid metric to test whether the present model can reproduce observations.

The procedure that we use is to spin up the model to steady state (this takes 20 model years) using $\alpha = 0.1$ and then run 24 consecutive 90-day simulations. The mean wind stress from each 90-day simulation has a large-scale component that has to be filtered out; this is achieved easily for these simulations by subtracting the known large-scale imposed stress field (i.e., from the case with $\alpha = 0$). This leaves just the small-scale contributions to wind stress, which we denote τ'. The mean SST from each case also has a large-scale component, but this is weak compared to local gradients and the results are insensitive to whether the SST data is spatially filtered. Thus, from each simulation we can calculate the wind stress divergence ($\nabla \cdot \boldsymbol{\tau}'$) and curl ($\nabla \times \boldsymbol{\tau}'$) as well as the SST gradients in the downwind ($\nabla {}^{o}T_m \cdot \boldsymbol{\tau}$) and crosswind ($\nabla {}^{o}T_m \times \boldsymbol{\tau}$) directions. Then, following the procedure established by Chelton et al. (2001), we

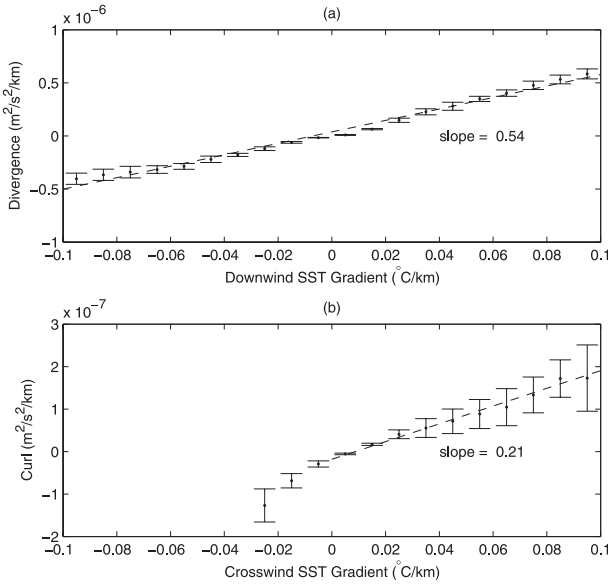

FIG. 1. Correlation between the local SST gradients and small-scale wind stress gradients for the case with $\alpha = 0.1$: (a) downwind SST gradient vs wind stress divergence and (b) crosswind SST gradient vs wind stress curl. Error bars show the standard deviation of the 24 simulations, and the slope has been converted to units of N m^{-2} °C^{-1} and multiplied by 100 to enable direct comparison with Chelton et al. (2004).

use the downwind (crosswind) temperature gradient at each data point to divide the wind stress divergence (curl) into bins and find the average within each bin. The same procedure applies to each 90-day segment, after which the mean and standard deviation of the 24 segments can be found. These results are shown in Fig. 1.

There are a number of striking similarities between the results shown in Fig. 1 and the satellite observations of the Kuroshio and Gulf Stream region (see Fig. 4 of Chelton et al. 2004). First, there is a roughly linear trend between divergence and the downwind SST gradient, and between the curl and the crosswind SST gradient. Second, the magnitude of the slope (calculated from a least squares fit and plotted by the dashed line) is similar to observations—for example, the slope of the divergence plot is 0.57, compared to 0.96 for the Kuroshio and 1.09 for the Gulf Stream (Chelton et al. 2004). Third, there is approximately a factor of 2 difference between the slope of the wind stress divergence and curl correlations, matching a ubiquitous feature of the observations. Finally, the error bars (an indicator of variability between the 90-day segments) are similar to observations. The one feature that differs from observations is the large bias in the calculation of crosswind SST gradient and wind stress curl. This result stems from

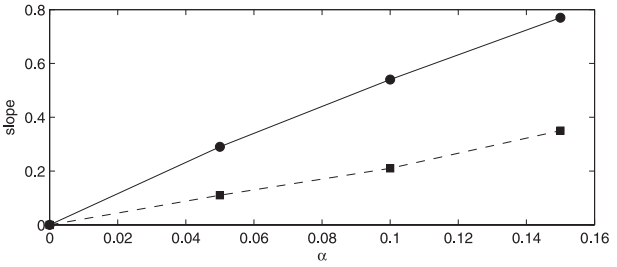

FIG. 2. Slopes from Fig. 1 as a function of the coupling coefficient α.

the steady zonal geostrophic wind field imposed in this model, meaning that there are relatively few samples with a negative crosswind SST gradient. For this reason we only use positive values of the crosswind gradient in calculating the least squares fit.

The magnitudes of the correlations discussed above are half the observed values, implying that the coupling coefficient (α) is too low. For example, Fig. 2 shows that the correlations increase almost linearly with the coupling coefficient so that a value $\alpha \approx 0.2$ may give the closest match to observations. However, there are a number of other factors in the model that can affect this relationship, including the strength of the zonal winds, the SST diffusion, model resolution, and the parameterization of ocean–atmosphere heat flux. Furthermore, there is sufficient regional variability in the strength of wind stress correlations to indicate that an exact match with data should not be expected.

Thus, we contend that, while the simple parameterization used in the present model is not designed to represent all possible processes contributing to mesoscale wind stress variations, the statistical effect upon the ocean surface is sufficiently close to observations to justify its use.

e. Experiments

The model described above is used for a series of numerical experiments designed to isolate the effect of ocean–atmosphere coupling on the large-scale circulation through mesoscale variation of wind stress. The standard parameter set for all simulations is shown in Table 1. Each simulation was given a 20-yr spinup period, and then mean fields are accumulated over an 80-yr model run.

Initial experiments involve forcing by steady atmospheric winds and varying the strength of the wind stress feedback parameter α. In this study we allow α to vary between 0 and 0.15 to model the range of relevant parameters of the system. The results of these experiments are described in the following section.

TABLE 1. Standard parameters for simulations, divided into global ocean and atmosphere components.

Parameters	Value	Description
X, Y	3840 km	Square domain size
Δx	10 km	Horizontal grid spacing
$\lvert F_s' \rvert$	90 W m^{-2}	Amplitude of variable incoming radiation
f_0	1×10^{-4} s^{-1}	Mean Coriolis parameter
β	2×10^{-11} (ms)$^{-1}$	Coriolis parameter gradient
λ	35 W m^{-2} K^{-1}	Sensible and latent heat flux coefficient
$\Delta^o t$	30 min	Ocean time step
^oH_k	(300, 1100, 2600) m	Ocean layer heights
^oH_m	100 m	Ocean mixed layer height
$^o\rho$	1000 kg m^{-3}	Ocean density
^oC_p	4000 J kg^{-1} K^{-1}	Ocean specific heat capacity
g_k	(0.05, 0.025) m s^{-2}	Reduced gravity
A_4	2.0×10^{10} m^4 s^{-1}	Biharmonic horizontal viscosity coefficient
$\alpha_{\rm bc}$	0.5	Mixed boundary current coefficient
$\delta_{\rm Ek}$	1 m	Bottom Ekman-layer thickness
$^oK_2$, $^oK_4$	380 m^2 s^{-1}, 4×10^{10} m^4 s^{-1}	Ocean diffusion coefficients
$^or_{dk}$	(51, 32) km	Ocean baroclinic Rossby radii (derived)
$\Delta^a t$	1 min	Atmosphere time step
^aH_m	1000 m	Atmosphere mixed-layer height
$^a\rho$	1 kg^{-1} m^{-3}	Atmosphere density
^aC_p	1000 J kg^{-1} K^{-1}	Atmosphere specific heat capacity
C_D	1.3×10^{-3}	Drag coefficient
$^aK_2$, $^aK_4$	2.7×10^4 m^2 s^{-1}, 3×10^{14} m^4 s^{-1}	Atmosphere diffusion coefficients

3. Results

a. Temperature-independent wind stress forcing case ($\alpha = 0$)

The model is forced by prescribed atmospheric velocity, which is a function of y only, as shown in Fig. 3a. The velocity field is designed to be slightly asymmetric so that the maximum velocity occurs about 200 km south of the center of the domain [to avoid the artificial symmetry of the QG equations; see Berloff and McWilliams (1999)]. For this case, with $\alpha = 0$, wind stress and Ekman-pumping velocity are also simple functions of y and are shown in Figs. 3b and 3c.

The time-mean SST and circulation in the upper layer of the ocean resulting from this steady forcing is shown in Figs. 4a and 4b. These figures describe a turbulent double-gyre circulation, which has been well characterized in the literature (e.g., Holland 1978): the western boundary current, inertial recirculations, and a strong eastward jet separating the two gyres are superimposed on a Sverdrupian background circulation. The jet has a very strong SST gradient, which plays no dynamical role in this experiment (as $\alpha = 0$) but has the potential to alter the forcing at finite α. The slight asymmetry in the forcing field is responsible for a shift in the jet to the south of the zero wind-stress curl line and some weak meanders in the jet.

The instantaneous fields (Figs. 4c,d) show the strong mesoscale activity in this parameter regime. The mean flow is strongly overprinted by geostrophic turbulence, which plays a key role in controlling both the mean state and low frequency variability of the system (Hogg et al. 2005; Berloff et al. 2007a). This mesoscale activity is also reflected in the SST field, producing a very intense front across the jet and additional small fronts in the interior of the flow. It is reasonable to expect that these fronts will play a role in determining the mean circulation at finite α.

b. Temperature-dependent wind stress forcing (nonzero α)

We now conduct simulations with the same prescribed atmospheric winds but with the inclusion of temperature-dependent wind stress. We show results from three simulations using $\alpha = 0.05, 0.10, 0.15$ in Fig. 5. The structure of the large-scale double-gyre circulation in these simulations shows clear differences from that in Fig. 4b. The temperature-dependent wind stress acts to substantially shorten the mean length of the jet dividing the two gyres while also enhancing meanders in the jet and reducing the strength of the inertial recirculations.

Figure 5d shows the variation of jet strength as a function of α. Here the maximum zonal velocity in the jet is plotted as a function of x in each case. The effect of increasing α is shown to clearly and systematically reduce the maximum jet velocity and to shorten the jet. Combination of these two effects provides a simple metric to allow comparison between different experiments in the following sections.

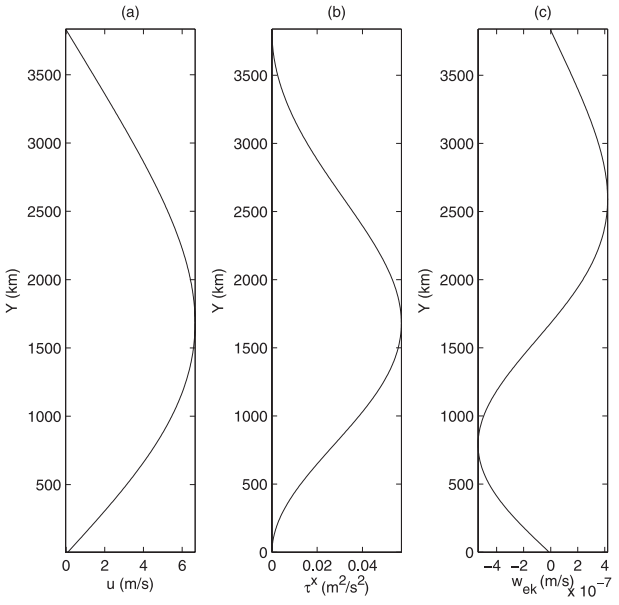

FIG. 3. Forcing as a function of latitude for the case with temperature-independent forcing ($\alpha = 0$): (a) prescribed atmospheric wind field ${}^a u_1$; (b) zonal component of stress in the atmospheric mixed layer; (c) ocean Ekman-pumping velocity.

This result leads to the obvious question: what elements of the temperature-dependent wind stress scheme are responsible for the gross changes in behavior of the double-gyre circulation? We now analyze this question in the context of several different hypotheses to show that the time-dependent small-scale forcing in the western boundary current separation region is responsible for the primary changes to the circulation.

In this model, α affects the ocean circulation through modifications to the wind stress and ocean Ekman-pumping velocity; see Eqs. (13) and (14). The time-mean of both components of wind stress and the Ekman pumping for the case with $\alpha = 0.1$ are plotted in Figs. 6a–c. The zonal wind stress (Fig. 6a) is enhanced over the western boundary of the subtropical gyre and reduced over the corresponding region of the subpolar gyre. In addition, there are changes to wind stress in the ocean interior, primarily along the core of the jet where SST fronts are common. The meridional wind stress (Fig. 6b) is due to atmospheric Ekman transport within the atmospheric mixed layer [see Eq. (12) for the generation of meridional velocity within the atmospheric mixed layer], and thus is directly proportional to zonal stress and $O(0.1\tau^x)$ in magnitude. The stress changes near the western boundary produce strongly positive Ekman-pumping anomalies over western edge of the subtropical/subpolar gyre (Fig. 6c). In the interior, gradients in wind stress along the eastward jet generate maxima in Ekman-pumping anomalies along the core of the jet; these maxima are an order of magnitude larger than the background Ekman pumping but are confined to a small region. Finally, we also show the standard deviation in Ekman-pumping velocity (Fig. 6d). This shows that the standard deviation (with a maximum of 10^{-5} m s^{-1}) is a factor of 20 greater than the background maximum Ekman pumping for the temperature-independent stress case (see Fig. 3c), indicating that extremely large instantaneous values of Ekman pumping occur in this simulation.

The simplest explanation for the large-scale impact of temperature-dependent wind stress would be the role of changes to the time-mean forcing. However, the turbulent double-gyre circulation is a nonlinear flow in which interaction between small-scale eddies and the large-scale flow controls the circulation. For example, eddies alter the mean flow either by mixing quantities, such as potential vorticity (PV), between the gyres or, alternatively, act to sharpen gradients in PV between the gyres through upgradient PV flux (see Berloff et al. 2007a). Furthermore, eddies are a product of instabilities of the mean circulation. This eddy–mean flow interaction implies that careful investigation of both the eddy field and the mean flow is needed to determine the controlling dynamics of this flow.

The spatial variation of the eddy field as a function of α is shown in Fig. 7. Here we compare the zonal spatial variation of mean kinetic energy along the jet with eddy kinetic energy in the jet region. The mean kinetic energy in the jet monotonically reduces with α, consistent with the data shown above. However, eddy kinetic energy increases with α near the western boundary current separation region, with a much faster decay in the zonal direction. In other words, very high eddy kinetic energy is induced by the temperature-dependent wind stress, but this is confined to the western boundary region.

The dynamical role of eddies in reducing the circulation strength with α can be investigated using the gyre-wide budget of PV. These are evaluated as an average over the closed (mean) streamlines of the subtropical gyre, following Berloff et al. (2007a), and yield the relative flux of PV into and out of the gyre from wind stress curl, eddy fluxes, and diffusive flux. Here we do not discriminate between diffusive flux of PV through the boundary and diffusive intergyre flux, but Berloff et al. (2007a) have shown that boundary fluxes dominate the diffusive flux in this turbulent parameter regime.

The PV budgets for the $\alpha = 0$ and $\alpha = 0.1$ cases are shown in Table 2. (Here our sign convention is such that a positive PV flux equates to an input of PV into the subtropical gyre.) Introduction of the temperature-dependent wind stress both reduces the amplitude of the wind stress curl (a positive PV input) and increases the eddy flux

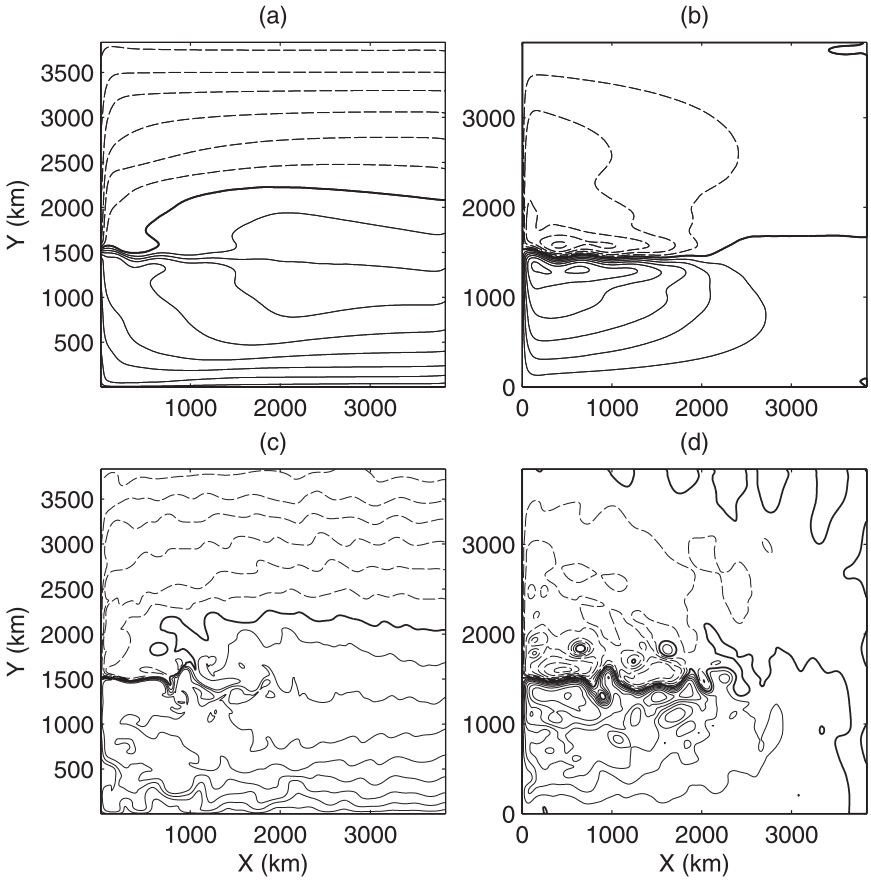

FIG. 4. Results for experiment with temperature-independent wind stress forcing: (a) mean SST field (relative to domain-averaged temperature; contour interval 2°C); (b) mean upper-layer streamfunction [CI 2 Sv (Sv $\equiv 10^6$ m^3 s^{-1})]; (c) instantaneous SST field at year 20; (d) instantaneous streamfunction at year 20. Negative contours are shown with a dashed line, zero contour with a bold line.

between the gyres. Both of these effects act to weaken the gyre. The change in wind forcing is due to a combination of a change in gyre shape and local Ekman pumping. The diffusive PV flux decreases correspondingly, presumably due to a weaker western boundary current, which leads to smaller PV gradients close to the western wall (data not shown).

The cumulative eddy flux of PV between the subtropical and subpolar gyres can be mapped as a function of longitude, as shown in Fig. 8. It is interesting to note that, despite the enhanced EKE near the western boundary in the finite α cases, the flux of PV in that region is not significantly altered. Instead, the primary difference between the two simulations shown is that, at small or zero α, the longer jet provides a larger barrier to the transport of PV between the gyres. In this region, PV flux is upgradient (negative), and the small α cases therefore result in weaker PV flux between the gyres.

This result demonstrates the subtleties involved in modeling turbulent double-gyre circulations. The strong dependence of the mean circulation upon the parameter α can be partially ascribed to the PV forcing, but this result does not uniquely determine the dynamical cause. The gyre dynamics is also governed by transport of PV between the gyres by eddies, which are themselves closely coupled to the strength of the circulation. For this reason, it is not clear from the above diagnosis whether the mean forcing is of sufficient magnitude to produce the observed changes. Instead, we frame two possible hypotheses to explain the effect of temperature-dependent wind stress. These hypotheses can then be explicitly tested with additional simulations.

1) HYPOTHESIS 1

The mean circulation is controlled by time-mean PV input. Thus, changes in Ekman pumping act to modify the total PV input to, and dynamics of, both gyres. The

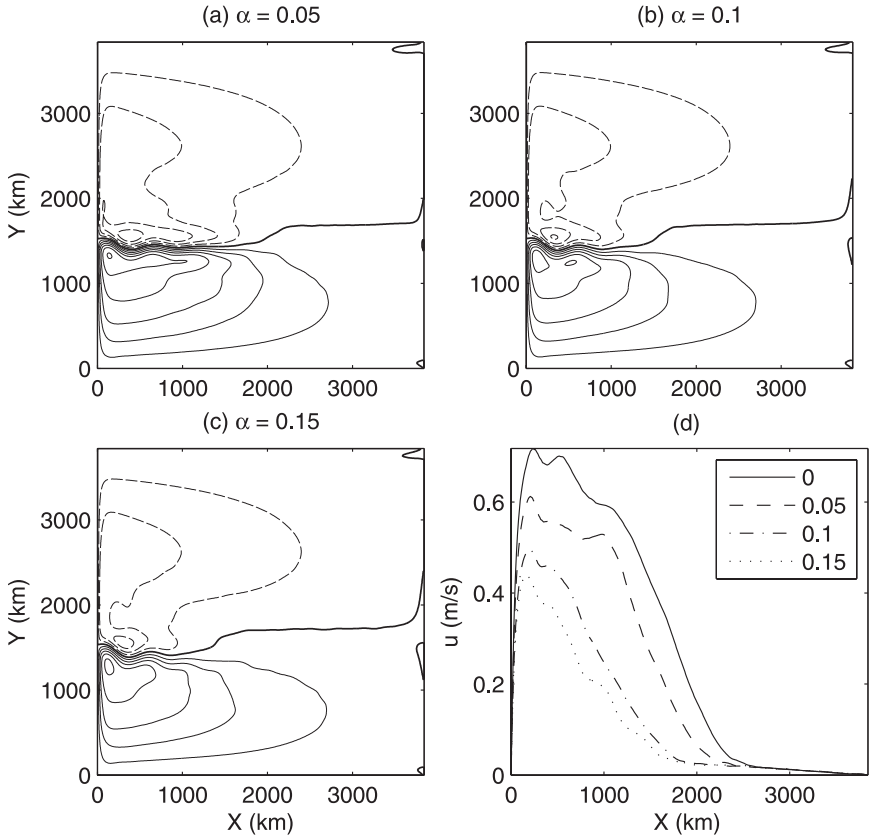

FIG. 5. Mean upper-layer streamfunction (CI 2 Sv) for (a) $\alpha = 0.05$, (b) $\alpha = 0.1$, and (c) $\alpha = 0.15$, and (d) maximum zonal velocity as a function of x along the jet core for varying α.

Ekman pumping may be dominated by broadscale changes affecting the gyrewide budget. Alternatively, large values of Ekman pumping very close to the jet may act to modify the jet dynamics so that both inertial recirculations and the jet are weakened. Under this scenario the changes in eddy activity are assumed to be a dynamical consequence of changing the mean PV balance of the gyres.

2) HYPOTHESIS 2

The time-dependent variability of the Ekman pumping is what modifies the circulation structure. This may occur via several mechanisms, namely 1) variable Ekman pumping acts as a random forcing of large-scale circulation, either directly by adding to the mesoscale-eddy random forcing (Berloff 2005a,b) or indirectly by destabilizing the flow (Spall 2007a) and thus enhancing mesoscale eddy forcing variance or 2) the essential part of Ekman-pumping variability is due to its correlation with the position of the variable oceanic jet. Under this scenario, it is the mean circulation that alters in response to Ekman-driven changes in the eddy field.

Both of these hypotheses are plausible but also independently testable using the model formulated here.

4. Additional experiments

a. Mean forcing experiments

We now perform a number of additional simulations to investigate the primary cause of changes to the double-gyre circulation due to the inclusion of temperature-dependent wind stress. First, we test hypothesis 1: that changes in the mean forcing control the large-scale response of the system. We achieve this by defining the time-mean atmospheric wind stress from the case with $\alpha = 0.1$, and denote this $\langle \tau_{\alpha=0.1} \rangle$. Then we force the ocean component of the model with this field replacing ${}^{a}\tau$. Simulations are integrated for 80 model years and compared with the $\alpha = 0$ and $\alpha = 0.1$ cases (Figs. 4b and 5b, respectively).

The ocean state (Fig. 9a) shows a double-gyre circulation that resembles the temperature-independent forcing case (Fig. 4b). The zonal velocity profile of the

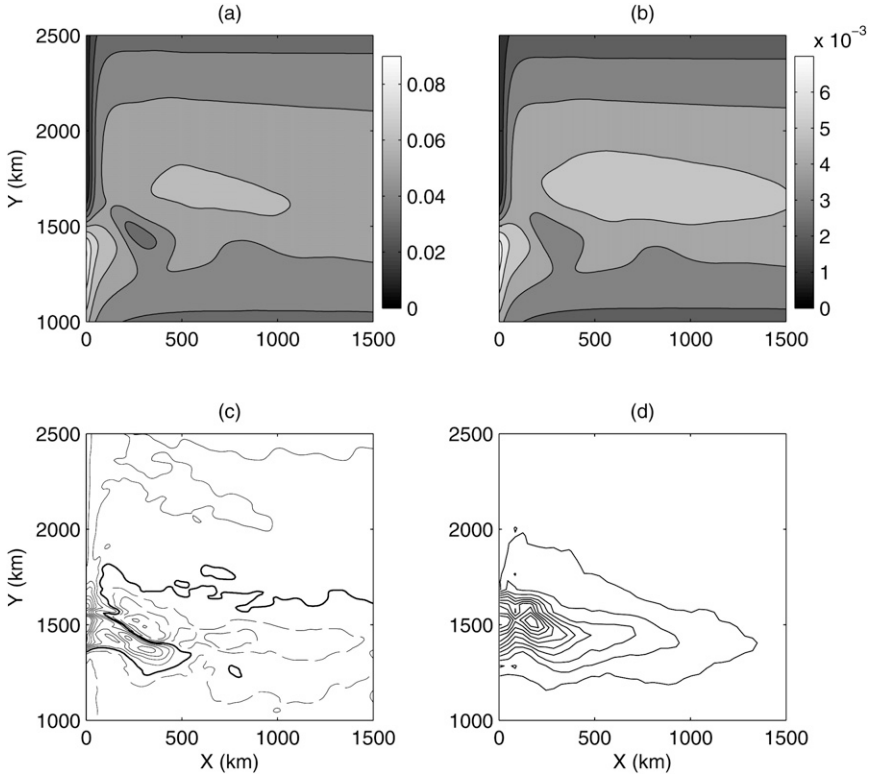

FIG. 6. Forcing fields for the temperature-dependent forcing case ($\alpha = 0.1$) concentrating on a small region of interest around the ocean jet: (a) mean zonal wind stress field (CI 0.01 m^{-2} s^{-2}); (b) time-mean meridional wind stress field (CI 0.001 m^{-2} s^{-2}); (c) time mean Ekman-pumping velocity (CI 4×10^{-7} m s^{-1}); and (d) standard deviation of ocean Ekman-pumping velocity (CI 1×10^{-6} m s^{-1}).

jet (solid line in Fig. 9e) is 200 km shorter and 15% slower than the temperature-independent case, but these changes are small when compared with the full temperature-dependent case (gray dashed line in Fig. 9e). We conclude that the mean wind stress curl cannot be responsible for the primary circulation changes induced by the temperature-dependent wind stress scheme, implying that hypothesis 1 above does not account for the first-order effect of temperature-dependent wind stress on the system. Nonetheless, there is a quantifiable difference between the present simulations and the temperature-independent case, which deserves some attention. In particular, we raise the question of whether interior or western boundary forcing dominates the response to mean forcing changes.

The roles of interior and western boundary forcing are separated by isolating two spatial modes of the forcing. We do this by defining the difference in wind stress between the temperature-dependent and the temperature-independent cases,

$$\Delta\tau = \langle\tau_{\alpha=0.1}\rangle - \langle\tau_{\alpha=0.0}\rangle. \tag{15}$$

We then write the western boundary component of this forcing difference as a separable function, $\Delta\tau^{\mathrm{WBC}} = \Delta\tau(x = 0)e^{-x/L}$, where L is chosen to maximize the fit with the pattern of $\Delta\tau$ near the western boundary. This allows us to define two new mean forcing fields; $\langle\tau^{\mathrm{WBC}}_{\alpha=0.1}\rangle = \langle\tau_{\alpha=0.0}\rangle + \Delta\tau^{\mathrm{WBC}}$ for the western boundary forcing, and $\langle\tau^{\mathrm{INT}}_{\alpha=0.1}\rangle = \langle\tau_{\alpha=0.1}\rangle - \Delta\tau^{\mathrm{WBC}}$, which represents only changes to forcing in the ocean interior. These fields are used to drive two additional simulations, with results shown in Figs. 9b and 9c, respectively.

These two cases highlight the nonlinearity of the turbulent double-gyre circulation. Neither simulation shows a measurable reduction in maximum velocity from the temperature-independent forcing case, and the jet length for the $\langle\tau^{\mathrm{WBC}}_{\alpha=0.1}\rangle$ case slightly exceeds the original. However, there is a reduction in the jet length of about 100 km in the $\langle\tau^{\mathrm{INT}}_{\alpha=0.1}\rangle$ case, implying that the pattern of Ekman pumping on either side of the jet plays some role in shortening the jet, while the western boundary contribution to forcing has very little effect on its own. The two effects combine nonlinearly to slightly weaken the jet, but that effect is minor compared with

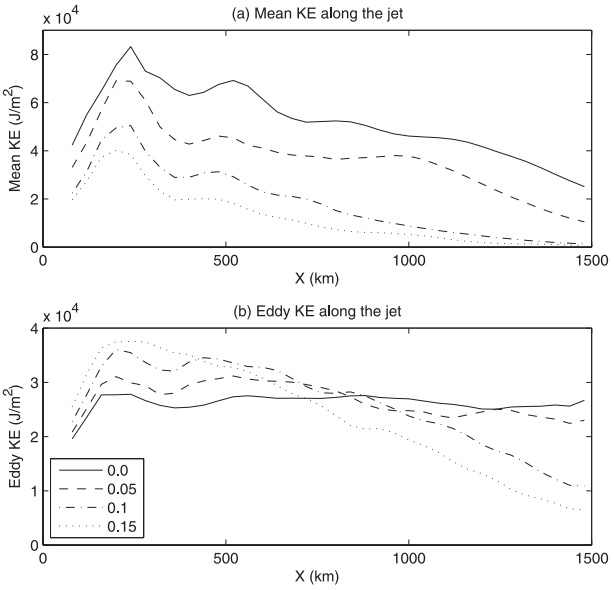

FIG. 7. (a) Mean kinetic energy and (b) eddy kinetic energy averaged across a band 200 km on either side of the jet as a function of zonal position.

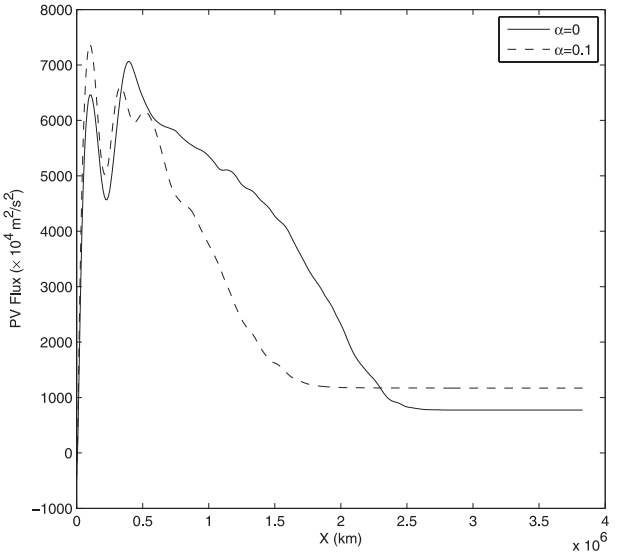

FIG. 8. Cumulative eddy PV flux as a function of zonal position along the intergyre boundary of the mean field. Positive flux near the western boundary represents a downgradient exchange of PV between the gyres, while the negative slope in the jet region represents an upgradient flux.

the temperature-dependent wind stress cases. This result implies that it is primarily the temporal variability of Ekman-pumping anomalies (hypothesis 2 above) that dominates the system response, and we now proceed to conduct numerical experiments to confirm this assertion.

b. *Variable forcing experiments*

Hypothesis 2 focuses not on the spatial pattern of mean forcing but on the temporal variability of the transient component of the forcing. We now aim to establish the exact role of forcing variability by separating the variability from the mean. This is achieved by synthesizing a new forcing field based on averages from the previous simulations. Specifically, we calculate wind stress forcing (for nonzero α), through Eq. (13), and then modify the forcing through

$$\tau^{\mathrm{VAR}} = \tau - \Delta\tau, \tag{16}$$

where $\Delta\tau$ is the difference in mean forcing from the two references cases as described above. In this case, the mean wind stress of the forcing, $\langle\tau^{\mathrm{VAR}}\rangle$, approaches the stress for the temperature-independent case, $\langle\tau_{\alpha=0.0}\rangle$, but the temporal and spatial variance of the forcing from the temperature-dependent case is retained.

TABLE 2. Mean potential vorticity forcing of the subtropical gyre ($\times 10^4$ m^{-2} s^{-2}).

	$\alpha = 0$	$\alpha = 0.1$
Wind forcing	−7160	−7010
Eddy intergyre flux	770	1170
Diffusive flux	6390	5840

The resulting time-mean circulation is shown in Fig. 9d. The shortened jet and large meanders of this simulation are very similar to the temperature-dependent wind stress case (Fig. 5b). In addition, the zonal velocity profile (dashed black line in Fig. 9e) shows markedly weaker velocities than the mean forcing simulations and is only a few percent greater than the full temperature-dependent case.

Figure 9e summarizes the results from each of the experiments described above and shows clearly that the primary effect of the temperature-dependent wind stress scheme on the jet length and velocity is unambiguously due to changes in the forcing variability, rather than the mean forcing. Applying the mean forcing from the $\alpha = 0.1$ case shortens the jet by about 200 km (compared with the $\alpha = 0$ case). Separating this into a WBC and interior component demonstrates the nonlinearity of the system in that neither of these experiments nor their average equals the mean forcing case, but that it is most likely that the interior forcing is more effective than the boundary forcing. However, these changes are small compared to the temperature-dependent case and the variable forcing case, where the jet is shortened by approximately 1000 km (nearly half its original length) and is 35% weaker. Given that the time-mean wind stress of the variable forcing case is almost identical to the temperature-independent

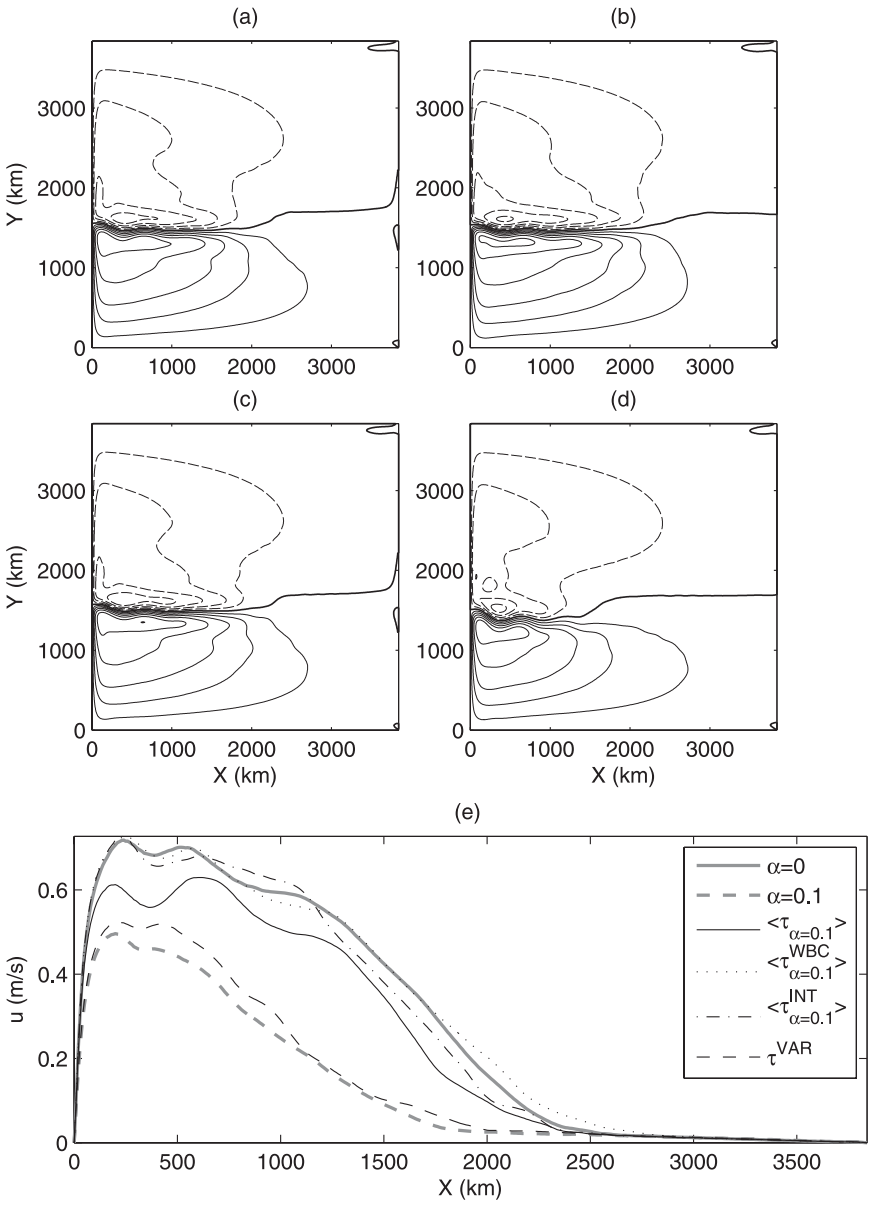

FIG. 9. Mean upper-layer streamfunction (CI 2 Sv) for (a) case forced with $\langle \tau_{\alpha=0.1} \rangle$, (b) case forced with $\langle \tau^{\mathrm{WBC}}_{\alpha=0.1} \rangle$, (c) case forced with $\langle \tau^{\mathrm{INT}}_{\alpha=0.1} \rangle$, and (d) case forced with τ^{VAR}; (e) maximum zonal velocity as a function of x along the jet core for these four experiments.

forcing case, this result provides strong support for hypothesis 2: that the temporal variability in wind stress curl forcing is responsible for the primary mesoscale coupling effect of the temperature-dependent wind stress scheme.

c. *Variance-modified experiments*

The role of eddy forcing variance in these simulations is now modified to test which characteristics of the variance are essential to controlling the flow. In particular, Berloff (2005b) shows that the space–time correlations of random forcing are important to the overall effect, and we now proceed to investigate this in the current model. In this context we ask the question: is the correlation between jet position and forcing required? In other words, does it matter whether a SST front causes forcing variance locally, or at another location?

We address this question with a numerical experiment in which forcing is specified rather than calculated from the coupled fields. The specified forcing comes from the forcing history of a 10-yr segment of the temperature-dependent case ($\alpha = 0.1$) for which ocean

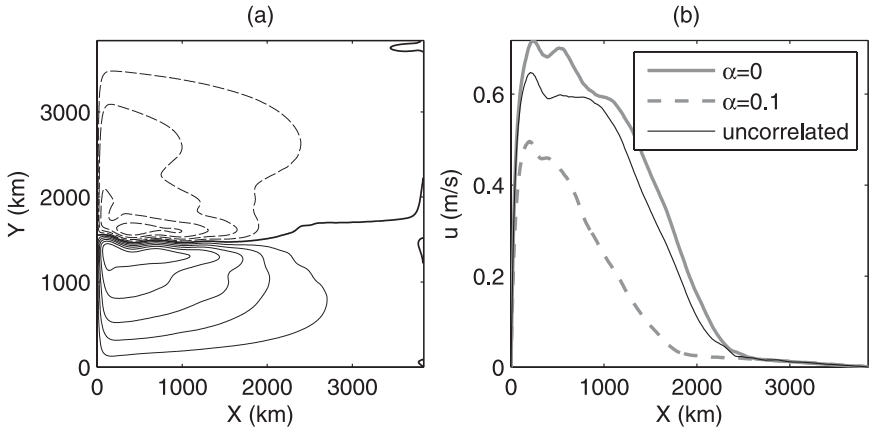

FIG. 10. Mean upper-layer streamfunction (CI 2 Sv) for (a) uncorrelated forcing without the correlation between ocean state and forcing variance and (b) maximum zonal velocity as a function of x along the jet core for the uncorrelated case, compared with the two reference cases.

Ekman pumping has been saved at daily intervals. This forcing field is used for an 80-yr simulation using a different initial state. In this experiment, the position of strong forcing will be spatially uncorrelated with the ocean fronts, but the statistics (mean and variance) of the forcing are identical to the original run. We call this simulation the ''uncorrelated'' case.

The results from the uncorrelated simulation are shown in Fig. 10, again in the form of the mean double-gyre circulation. The time-mean state shows a long, straight jet that is only slightly weaker than the temperature-independent case. This simulation demonstrates that not only is the variability of the forcing important but also the correlation between variable forcing and the flow state plays a role in the effect of the temperature-dependent wind stress. It remains to discern the relevant nature of those correlations, determine why they alter the flow state so significantly, and whether this dynamical effect is likely to play a role in determining the real ocean circulation.

An additional test on this system is to examine whether the role of Ekman-pumping anomalies is local or gyrewide. For example, one could argue that the integrated PV input to the time-dependent gyre is more relevant to the flow state than the PV input to the time-mean gyre. We test this idea by running two further simulations. In the first simulation the component of forcing due to the temperature-dependent stress effect is averaged over the instantaneous time-dependent subtropical gyre and distributed evenly over the gyre. In general, this represents a weakening of the forcing and may result in a weakening of the circulation. A complementary test is one in which the gyrewide forcing anomalies are compensated for by a uniform additional value, but the localized time-dependent forcing near the jet is retained. These two simulations are called the ''redistributed'' and ''local'' tests respectively in Fig. 11. The results in this case are again unambiguous. It is the localized time-dependent forcing near the ocean jet that acts to weaken the circulation. Thus, we conclude that localized correlations between the time-dependent forcing and flow state are of critical importance to the effects observed here.

d. Low-order model

The role of mesoscale wind stress variability is now clarified using a low-order model for the temperature-dependent stress parameterization. The goal is to represent the wind stress variability using ocean flow variables only. To do this we note that the wind stress curl—the driving term in Eq. (1)—depends linearly on the cross-wind temperature gradients in both the numerical experiments (Fig. 1b) and observations. Furthermore, SST is negatively correlated with PV (and relative vorticity) in the WBC separation region. Thus we propose that the dynamical effect of temperature-dependent wind stress forcing in this model may be captured by a simple parameterization scheme that assumes a linear relationship between the meridional vorticity gradient and Ekman-pumping anomalies. We choose a parameterization based on the relative vorticity gradient (rather than the PV gradient) under the assumption that relative vorticity dominates PV on smaller scales (and has the advantage that it eliminates the β effect). Thus we write

$$w_{\mathrm{Ek}} = \overline{w_{\mathrm{Ek}}} + \gamma \frac{\partial}{\partial y}(\nabla_H^2 p_1), \tag{17}$$

where $\overline{w_{\mathrm{Ek}}}$ is the wind stress curl calculated from (14) with $\alpha = 0$ and γ is an empirical factor tuned using the

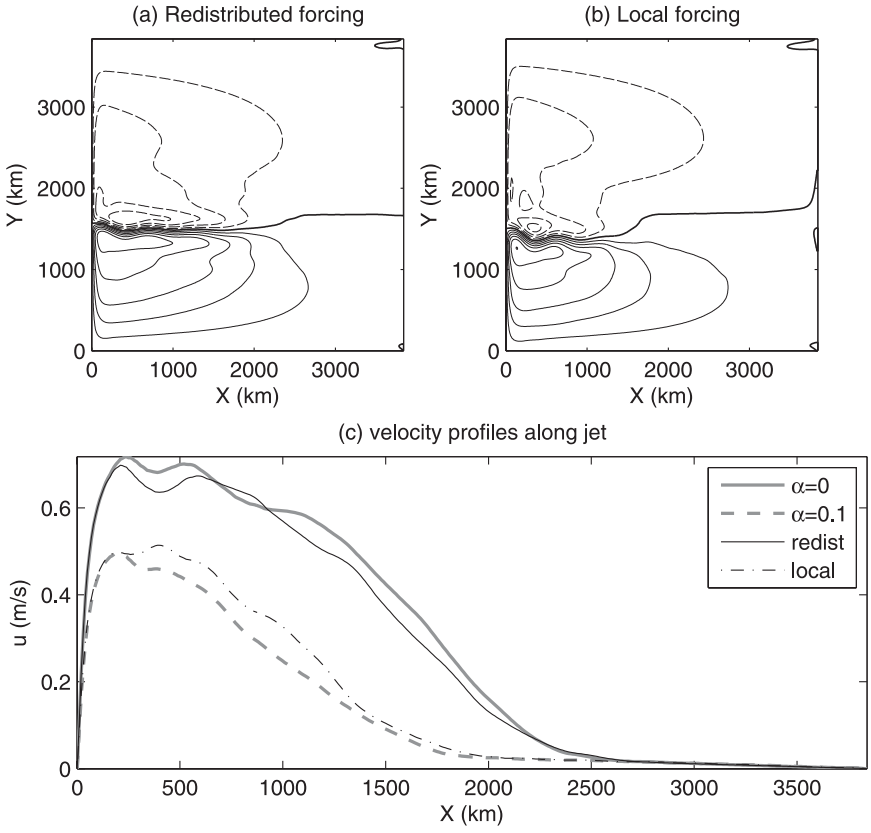

FIG. 11. Mean upper-layer streamfunction (CI 2 Sv) for (a) redistributed forcing case in which PV forcing anomalies are distributed across the entire time-dependent gyre, (b) local forcing in which redistribution is used to ensure that the gyrewide PV input is equal to the time-mean PV forcing, and (c) maximum zonal velocity as a function of x along the jet core for the redistributed and local cases, compared with the two reference cases.

$\alpha = 0.1$ case to match the Ekman-pumping forcing there (we use $\gamma = 8 \times 10^7$ m^2 s, yielding maximum Ekman-pumping velocities of 2×10^{-5} m s^{-1}). Equation (17) is applied over all points except those within three grid points of the boundary (where high relative vorticity is due to boundary friction rather than fronts in the ocean interior) for a simulation without a dynamic mixed layer or explicit temperature-dependent stress.

The results for this simulation are shown in Fig. 12. The time-mean flow is faster than the $\alpha = 0.1$ case in the inertial part of the jet core, but jet length matches the temperature-dependent wind stress case to a surprising degree. The higher velocities in the jet core are most likely due to differences in the boundary Ekman pumping, which alters the PV distribution close to the western boundary current. However, the primary result of this simulation is that the parameterization described by (17) curtails the jet length in the same way as the temperature-dependent wind stress scheme, implying that the primary effect of the wind stress scheme on the mean circulation is due to small-scale correlations between forcing and the ocean flow state.

5. Discussion and conclusions

The numerical experiments described here are designed to determine the effect of temperature-dependent wind stress upon the large-scale ocean circulation in an eddy-resolving model. Temperature-dependence causes elevated wind stress in regions where strong fronts in SST (and PV) produce large gradients in the stress and, hence, large values of wind stress curl. In this model, where we have restricted the atmospheric winds to be time independent and purely zonal, and most fronts are oriented in the zonal direction, the dominant term is the ageostrophic northward Ekman transport in the atmospheric mixed layer that brings warm air across the front. The result is a strong atmosphere–ocean temperature difference north of the front, which, according to the parameterized temperature dependence of stress,

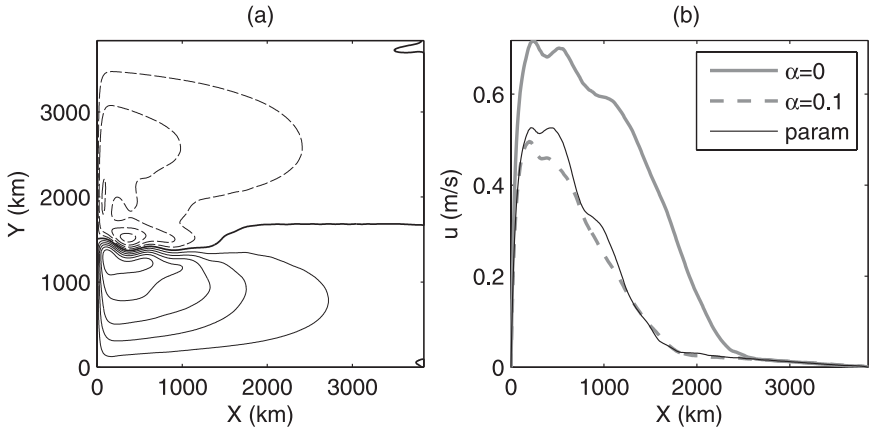

FIG. 12. (a) Mean upper-layer streamfunction (CI 2 Sv) and (b) maximum zonal velocity as a function of x along the jet core for the simulation using the parameterization described by (17).

produces strong wind stress curl from both components of the wind stress.

The above simulations show that the changes in wind stress due to temperature dependence can have a very strong effect on the circulation of the ocean in this eddy-resolving model. The effect is produced not by changes to the mean wind stress but is, instead, due to the temporal variations of stress. Moreover, we have shown that the correlation between the instantaneous flow state and the time-dependent stress is crucial in altering the circulation. This was demonstrated by comparing runs with the same forcing variability, but one of which had forcing prescribed from a previous simulation rather than part of the coupled calculation. As a result, a simple empirical parameterization of the flow state can replace the full coupled equation with some success.

The exact mechanism by which small-scale forcing terms near the jet modify the gyrewide circulation is not entirely clear from this study because of the coupled nature of the eddy forcing and the mean circulation. However, some clarification is provided by Table 2 and Fig. 8 with reference to the results of Berloff et al. (2007b). This data shows that the simulation with temperature-dependent stress included has both a smaller PV forcing from the wind field and a stronger eddy intergyre flux. The stronger intergyre flux is due to a weakening of the intergyre PV barrier, implying that the jet dividing the two gyres is destabilized by the small-scale wind forcing in this region. Enhanced baroclinic instability was predicted by Spall (2007a) for the case of poleward airflow over a front; however, the mechanisms proposed by Spall do not appear to be active in this flow.

We have used a suite of experiments to eliminate a number of plausible hypotheses for the system behavior. The final result is that we know that the small-scale forcing near the ocean jet is critical. This forcing can be parameterized as a linear function of the gradient of relative vorticity, acting to produce intense positive Ekman pumping over regions of strong fronts. The primary effect of positive Ekman pumping is to attract fronts, including the primary jet dividing the two gyres, to the south. We propose that this southward movement acts to destabilize the jet—either by tilting the jet in a southeasterly direction or by creating a large meander near the western boundary separation point (which is controlled independently). The effect on the system is thus high EKE near the western boundary (Fig. 7) and a shorter jet, which results in a weaker PV barrier between the gyres and thus a weaker circulation in total.

The results in this study pertain to a particular, idealized, numerical model of the ocean. It remains to determine whether such an effect will be equally significant in the real ocean. We do not directly answer this question in the present paper but, instead, make the case that the effect seen here is a potentially important part of the ocean–atmosphere system and that it deserves additional attention. In particular, we used scatterometer observations to demonstrate that the temperature-dependent wind stress scheme produced realistic effects, but there are significant uncertainties in the estimate of the best value of the coupling coefficient to use. Thus, process modeling and observations of the ocean and atmospheric boundary layer are needed to better constrain the magnitude of wind stress forcing changes. Furthermore, the present simulations used a purely zonal geostrophic wind field; simulations using a model with time-dependent winds, including synoptic events, may result in significantly greater effects due to a nonzonal geostrophic wind over SST fronts. The present study is idealized in many respects: simulations with large-scale, high-resolution ocean–climate models are needed to gauge the overall effect of temperature-dependent wind stress on the ocean.

Scatterometer studies also show the emergence of small-scale stress variability due to differences between oceanic and atmospheric velocity (Chelton et al. 2004; Park et al. 2006). This effect was not included in the present simulations. Additional tests (not shown here) indicate that this component of small-scale stress does not alter the mean circulation significantly for the double-gyre case, but can do so in the case of a channel ocean (mimicking the Antarctic Circumpolar Current). This is the subject of ongoing work.

The results shown here also have implications for the forcing of eddy-resolving ocean models. The importance of small-scale wind stress curl may lead one to assume that realistic forcing [e.g., directly importing Quick Scatterometer (QuikSCAT) wind stress data] will produce a mean circulation closer to observations. However, unless the model is a perfect representation of reality, such a forcing strategy will miss the mesoscale effects seen here because the correlation between flow states and forcing anomalies will be absent (Seo et al. 2007). Therefore, we propose that eddy-resolving models require forcing by large-scale winds, with an additional high-resolution dynamic mixed layer (or parameterization) to represent the mesoscale coupling effect.

The existence of temperature-dependent wind stress has been noted by several previous studies. However, the effect is small scale and, perhaps, assumed by many to be local. This study has demonstrated the opposite—that small-scale forcing of the ocean can produce large-scale effects. Specifically, we find that

1) Including a temperature-dependent wind stress scheme with realistic magnitude in an eddy-resolving ocean model substantially changes the time-mean circulation.
2) The primary effect in this model is due to ageostrophic meridional Ekman transport of the atmospheric mixed-layer temperature, which acts to produce a local intense wind stress curl close to fronts.
3) This local forcing enhances turbulence in the region of the jet separation by destabilizing the flow and reduces the upgradient eddy flux farther downstream. The resulting mean circulation consists of weaker gyres and a weaker jet.

The implication is that the next generation of eddy-resolving ocean–climate models will either need to parameterize, or else directly simulate, the effects of mesoscale coupling due to ocean–atmosphere interactions on the scale of the oceanic Rossby radius.

Acknowledgments. AH and WD were supported by an ARC Linkage International Grant (LX0668781). WD was also supported by NSF Grants OCE 0424227 and OCE 0550139. Funding for PB was provided by NSF Grants OCE 0344094 and OCE 0725796 and by the research grant from the Newton Trust of the University of Cambridge. SK was supported by U.S. DOE Grant DE-FG02–02ER63413 and NASA Grant NNG-06-AG66G-1. Numerical computations were supported by an award under the Merit Allocation Scheme on the National Facility of the Australian Partnership for Advanced Computing.

REFERENCES

Berloff, P. S., 2005a: On rectification of randomly forced flows. *J. Mar. Res.,* **63,** 497–527.

——, 2005b: Random-forcing model of the mesoscale oceanic eddies. *J. Fluid Mech.,* **529,** 71–95.

——, and J. C. McWilliams, 1999: Large-scale, low-frequency variability in wind-driven ocean gyres. *J. Phys. Oceanogr.,* **29,** 1925–1949.

——, W. Dewar, S. Kravtsov, and J. McWilliams, 2007a: Ocean eddy dynamics in a coupled ocean–atmosphere model. *J. Phys. Oceanogr.,* **37,** 1103–1121.

——, A. M. Hogg, and W. Dewar, 2007b: The turbulent oscillator: A mechanism of low-frequency variability of the wind-driven ocean gyres. *J. Phys. Oceanogr.,* **37,** 2363–2386.

Chelton, D. B., and Coauthors, 2001: Observations of coupling between surface wind stress and sea surface temperature in the eastern tropical Pacific. *J. Climate,* **14,** 1479–1498.

——, M. G. Schlax, M. H. Freilich, and R. F. Milliff, 2004: Satellite measurements reveal persistent small-scale features in ocean winds. *Science,* **303** (5660), 978–983.

Cronin, M. F., S.-P. Xie, and H. Hashizume, 2003: Barometric pressure variations associated with eastern pacific tropical instability waves. *J. Climate,* **16,** 3050–3057.

Dewar, W., and G. Flierl, 1987: Some effects of the wind on rings. *J. Phys. Oceanogr.,* **17,** 1653–1667.

Haidvogel, D. B., J. C. McWilliams, and P. R. Gent, 1992: Boundary current separation in a quasigeostrophic, eddy-resolving ocean circulation model. *J. Phys. Oceanogr.,* **22,** 882–902.

Hogg, A. M., J. R. Blundell, W. K. Dewar, and P. D. Killworth, 2003a: Formulation and users'guide for Q-GCM (version 1.0). Southampton Oceanography Centre, Internal Doc. 88. [Available online at http://www.noc.soton.ac.uk/JRD/PROC/Q-GCM/q-gcmv1.0.pdf.]

——, W. K. Dewar, P. D. Killworth, and J. R. Blundell, 2003b: A quasi-geostrophic coupled model (Q-GCM). *Mon. Wea. Rev.,* **131,** 2261–2278.

——, P. D. Killworth, J. R. Blundell, and W. K. Dewar, 2005: Mechanisms of decadal variability of the wind-driven ocean circulation. *J. Phys. Oceanogr.,* **35,** 512–531.

Holland, W., 1978: The role of mesoscale eddies in the general circulation of the ocean: Numerical experiments using a wind-driven quasi-geostrophic model. *J. Phys. Oceanogr.,* **8,** 363–392.

Lindzen, R. S., and S. Nigam, 1987: On the role of sea surface temperature gradients in forcing low-level winds and convergence in the tropics. *J. Atmos. Sci.,* **44,** 2418–2436.

Liu, W. T., X. Xie, and P. P. Niiler, 2007: Ocean–atmosphere interaction over Agulhas extension meanders. *J. Climate,* **20,** 5784–5797.

Milliff, R. F., W. G. Large, W. R. Holland, and J. C. McWilliams, 1996: The general circulation responses of high-resolution north Atlantic Ocean models to synthetic scatterometer winds. *J. Phys. Oceanogr.,* **26,** 1747–1768.

Nonaka, M., and S.-P. Xie, 2003: Covariations of sea surface temperature and wind over the Kuroshio and its extension: Evidence for ocean-to-atmosphere feedback. *J. Climate,* **16,** 1404–1413.

O'Neill, L. W., D. B. Chelton, and S. K. Esbensen, 2003: Observations of SST-induced perturbations of the wind stress field over the Southern Ocean on seasonal time scales. *J. Climate,* **16,** 2340–2354.

——, ——, ——, and F. J. Wentz, 2005: High-resolution satellite measurements of the atmospheric boundary layer response to SST variations along the Agulhas return current. *J. Climate,* **18,** 2706–2723.

Park, K.-A., P. Cornillon, and D. L. Codiga, 2006: Modification of surface winds near ocean fronts: Effects of Gulf Stream rings on scatterometer (QuikSCAT, NSCAT) wind observations. *J. Geophys. Res.,* **111,** C03021, doi:10.1029/2005JC003016.

Pedlosky, J., 1987: *Geophysical Fluid Dynamics*. Springer-Verlag, 707 pp.

Samelson, R. M., E. D. Skyllingstad, D. B. Chelton, S. K. Esbensen, L. W. O'Neill, and N. Thum, 2006: On the coupling of wind stress and sea surface temperature. *J. Climate,* **19,** 1557–1566.

Seo, H., M. Jochum, R. Murtugudde, A. J. Miller, and J. O. Roads, 2007: Feedback of tropical instability-wave-induced atmospheric variability onto the ocean. *J. Climate,* **20,** 5842–5855.

Small, R. J., S.-P. Xie, and Y. Wang, 2003: Numerical simulation of atmospheric response to Pacific tropical instability waves. *J. Climate,* **16,** 3723–3741.

——, ——, ——, S. K. Esbensen, and D. Vickers, 2005: Numerical simulation of boundary layer structure and cross-equatorial flow in the eastern Pacific. *J. Atmos. Sci.,* **62,** 1812–1830.

——, and Coauthors, 2008: Air–sea interaction over ocean fronts and eddies. *Dyn. Atmos. Oceans,* **45** (3–4), 274–319.

Spall, M. A., 2007a: Effect of sea surface temperature–wind stress coupling on baroclinic instability in the ocean. *J. Phys. Oceanogr.,* **37,** 1092–1097.

——, 2007b: Midlatitude wind stress–sea surface temperature coupling in the vicinity of oceanic fronts. *J. Climate,* **20,** 3785–3801.

Sweet, W., R. Fett, J. Kerling, and P. La Violette, 1981: Air–sea interaction effects in the lower troposphere across the north wall of the Gulf Stream. *Mon. Wea. Rev.,* **109,** 1042–1052.

Xie, S.-P., 2004: Satellite observations of cool ocean–atmosphere interaction. *Bull. Amer. Meteor. Soc.,* **85,** 195–208.